Void distributions and permeability prediction for rotationally moulded polymers

B.R. Murray, S.B. Leen, C.M. Ó Brádaigh

Mechanical Engineering, National University of Ireland Galway, Ireland

ABSTRACT: An experimental study of void distributions for rotationally moulded polyethylene is presented. The effects of key variables such as maximum process temperature and nominal wall thickness (via powder mass) are studied. Analytical models and finite element mass diffusion models for the permeability of heterogeneous polymers with air voids are presented and comparatively assessed. The FE method allows modelling of realistic (measured) void distributions. A preliminary estimation method for void volume fraction and mean void radius is presented. This approach is based on hot plate measurements and is shown to give good correlation with the rotationally moulded material for different process temperatures. Key objectives of the present work are (i) to develop an understanding of the factors affecting gas permeability in rotationally moulded polymers and (ii) to develop experimental and computational methods to help design low permeability rotomoulded polymer liners.

1. INTRODUCTION

Composite overwrapped pressure vessels (COPVs) find many applications in satellite and space applications. Their ability to store highly permeating fuels at high pressures under cryogenic conditions makes them an integral part of propulsion systems, breathing systems and specialised research and analysis equipment aboard rockets, satellites and spacecraft [1, 2]. A COPV consists of two main components: a low permeability liner and a high strength fibre overwrap. Titanium and aluminium have become the predominant materials for liners due to their low permeability characteristics, resistance to chemical attack and high specific strength [3]. While titanium has traditionally been the preferred liner material for high end applications [4], its major drawback is cost [5]. Alternative COPV liner materials have been highlighted as an area of development for reducing costs while still providing an acceptable level of fuel containment [6]. This drive for increased efficiency and economical use of resources is the motivation for the present work.

Recent research has focused on the use of polymers as prospective liner materials with liquid crystal polymers, fluoropolymers and polyamides displaying beneficial characteristics for cryogenic fuel containment [7]. Recent industrial examples include injection blow moulding of a HDPE liner [8] and thermal welding of a fluoropolymer liner for similar applications [9]. The maximum permeation rate for COPV tanks depends on the application, fuel type and tank size. However, one recently quoted limiting value is 2.23×10^{-7} mol/s for an entire tank structure [8]. The methods used to manufacture polymer liners tend to be

expensive and time consuming. Injection blow moulding processes incorporate expensive mould tooling with intricate air pathways for cooling operations while also requiring preforming of the polymer liner prior to manufacturing [10, 11].

Recent studies have focused on the predicted permeability of the composite overwrap [12] while this paper presents a combined experimental and computational study on void distributions and predicted permeability for a rotationally moulded polymer liner. The experimental method employs hot plate manufactured samples and rotational moulding of a polymer liner demonstrator using an integrally heated rotomoulding tool. The key effects of moulding temperature and nominal wall thickness are quantified experimentally and a preliminary estimation method for the effect of moulding temperature on void distribution statistics is presented. A finite element (FE) mass diffusion model is developed to predict the effect of void distributions on liner permeability. The FE model is compared and validated against permeability from theoretical models for heterogeneous materials, adapted here to air void distributions in the polymer liner material.

Key objectives of the present work are (i) to develop an understanding of the factors affecting gas permeability in rotomoulded polymers and (ii) to develop experimental and computational methods to help design low permeability rotomoulded polymer liners. A specially ground polyethylene powder forms the base material for part production in the

present work, as detailed in Table 1. Pressurisation of the mould is not necessary during production and so moulds can be thin-walled, making them cheaper to produce and modify [13].

2. MASS DIFFUSION THEORY

2.1. Fick's Law

Attention is focused here on minimisation of mass transfer rates of helium across the polymer wall. Mass transfer rates for steady state analyses across wall sections are governed by Fick's first law of diffusion relating the mass flow rate *J* of the diffusing substance through a unit area cross section to the concentration gradient across that section [14, 15]:

$$J = -D\frac{\partial C}{\partial x} \tag{1}$$

where *D* is the diffusion coefficient of the material, *C* is the concentration, and x is the thickness of the sample (Fig. 1). Homogeneous plastics are known to have relatively low diffusion coefficients and hence low mass flow rates [16]. This is beneficial for fuel storage. However, depending on the manufacturing method employed, the permeability of real polymer components is affected by void growth resulting from processing. Air voids increase effective permeability, due to the diffusion coefficients for gases in air being higher than in the homogeneous polymer [17]. Hence, a higher air void volume fraction leads to a higher

mass flow rate as the voids act as leakage paths for the mass flow. It is important, therefore, to quantify the effect of mould process conditions such as temperature and wall thickness (or powder mass), on void distribution statistics.

The solubility coefficient *S* is used here to define the local concentration of diffused gas at the boundary of the polymer layer [17, 18]. The concentration *C* at the boundary is defined as the product of *S* and the partial pressure *P* of the gas on that side of interface.

2.2. Predictive Permeability Equations

For inhomogeneous materials, such as polymers with air voids, different diffusion coefficients apply to the continuous polymer and dispersed air void regions within the material cross section with the mass flow following the path of least resistance [19]. The basis for heterogeneous studies can be traced back to Maxwell who was the first to derive a relationship between a dispersed phase in a continuous matrix for electrical conductivity measurements using the potential theory for electrical conductance [20]. Maxwell developed an equation which related the permeability of both phases in the heterogeneous material to a relative permeability, P_r, for the entire material as follows:

$$P_r = \frac{P}{P_m} = \left[\frac{2(1-\phi) + (1+2\phi)\lambda_{dm}}{(2+\phi) + (1-\phi)\lambda_{dm}}\right] \tag{2}$$

where P is the effective permeability of the heterogeneous material, P_m is the permeability of the matrix and ϕ is the volume fraction of the dispersed phase in the matrix. λ_{dm} is defined as the permeability ratio between the dispersed phase, P_d, and the matrix material, P_m, with $\lambda_{dm} = P_d / P_m$. The Maxwell model is quite effective at determining permeabilities for lower volume fractions (ϕ<0.2) but its accuracy decreases significantly for higher volume fractions. This model does not account for the particle size, shape or distribution in the matrix and assumes that the particles are a collection of randomly distributed solid spheres with no interactions between dispersed particles [21].

The Bruggeman model [22] was originally developed for electrical conductivity purposes, but can be adapted to predict the permeability of dual phase materials by using the differential effective medium approach, to give the following equation:

$$(P_r)^{\frac{1}{3}}\left[\frac{\lambda_{dm}-1}{\lambda_{dm}-P_r}\right] = (1-\phi)^{-1} \qquad (3)$$

As with the Maxwell model, it utilises the same parameters to predict a relative permeability for the composite medium. The model faces similar problems in representing real materials in that it does not account for the particle size, shape, dispersion or interactions between particles. Eq. (3) is a non-linear equation and needs to be solved using iterative methods. In the present case, a Newton-Raphson approach is adopted.

The Lewis-Nielsen model [23, 24] can also be adapted to predict the permeability of heterogeneous polymers from its original purpose for predicting the elastic modulus of particulate composites, as follows:

$$P_r = \frac{P}{P_m} = \left[\frac{1 + 2\left(\frac{\lambda_{dm} - 1}{\lambda_{dm} + 2}\right)\phi}{1 - \left(\frac{\lambda_{dm} - 1}{\lambda_{dm} + 2}\right)\phi\psi}\right] \quad (4)$$

$$\psi = 1 + \left(\frac{1 - \phi_m}{\phi_m^2}\right) \quad (5)$$

This model is an improvement over those previously mentioned as it takes into account the maximum packing volume, ϕ_m, of particles within the matrix (ϕ_m = 0.64 for close packed spheres). This therefore allows for the particle size and shape to be accounted for within the composite and gives a better prediction for the overall permeability. It is also notable that the Lewis-Nielsen model reverts to the Maxwell model when the maximum packing volume of particles is equal to one (ϕ_m = 1) [21].

While these equations have been developed for alternative purposes such as heat transfer and electrical conductivity predictions, a number of authors have already used them for permeability predictions and comparisons to real data with good correlation being achieved depending on the model used and application tested [25 - 28]. These equations are

compared below to predicted values of permeability from three dimensional FE mass diffusion models, where the FE models explicitly include the random distributions of voids.

2.3. Finite element model

An FE based implementation of Fick's law is employed to study the steady-state mass diffusion behaviour of the polymer with random distributions of voids [29]. An idealised three dimensional model with cross sectional dimensions of 3mm x 1mm x 1 mm was developed as shown in Fig. 2. A Python scripting code was developed to define the random distribution of three-dimensional spherical voids (of uniform size), corresponding to a given void volume fraction. In the analyses presented below, and based on measured void sizes, void radii of between 100 μm and 200 μm are modelled. For a given set of processing conditions, the measured range of void radii was found to be quite small, so that the assumption of uniform void size is considered reasonable. This assumption also makes the mesh generation process more straightforward. The analyses were based on the use of helium as the diffusing gas based on a standard permeability test for plastic sheeting [30]. Also, there is a high safety risk associated with the use of hydrogen gas whereas helium is relatively non-reactive. Helium has a smaller molecular size than hydrogen [31 – 33], so that it is arguably more demanding basis for permeability assessment.

The FE model was used to study the effect of void volume fraction using ten different random distributions of voids for each value of volume fraction. These results are compared below to the results from the theoretical permeability models, which cannot include the effect of random distributions. The FE model was also used to study the effect of wall thickness (powder mass) on permeability. This study consisted of (i) a generic study of the effect of wall thickness for three different void volume fractions of 0%, 5% and 10%, all using a uniform void radius of 150 μm and (ii) three separate analyses corresponding to three different powder mass cases (R3, R4 and R5), all at 180 ^{o}C, of Table 2. The analyses of (i) are intended to demonstrate the effect of wall thickness for different void volume fractions. In contrast, the analyses of (ii) incorporate the combined effects of wall thickness variation (due to the different powder masses) and the associated measured void volume fractions (with a void radius of 150 μm). The analyses here used linear four node tetrahedral elements for the steady-state analyses. Other details used in the FE analysis are given in Table 3. A convergence study was carried out to establish convergence of the predicted mass flow rates with respect to element size. The finite element analyses conducted here utilise a 25 μm mesh size.

3. METHODOLOGY

3.1. Modified Rotational Moulding Process

Rotational moulding uses a biaxially rotating arm in conjunction with a polymer powder and the application of heat to produce a hollow part of uniform wall thickness. The entire process is conventionally contained within a large heating oven and involves four main steps as displayed in Fig. 3. These steps include placing the powder into the mould, melting the powder through the application of heat while the arm rotates coating the inside of the mould with the molten polymer, then cooling the mould to allow for solidification of the part and finally demoulding the part from the mould wall [34].

A modified rotational moulding process [35] was developed here to produce hollow polyethylene components by replacing the surrounding oven with an integrally-heated mould tool contained within the rotating axes as shown in Fig. 4. This image displays the rotational moulding equipment used, consisting of the two rotating axes and a box-shaped mould mounted in the centre of the inner axis. The dimensions of the inner rotating plane frame are approximately 2.5 m x 2.5 m allowing for the moulding of parts with large dimensions. All electronics and controls are transmitted across the different axes through the use of slip rings at the main rotating joints which allow for electrical heating of the mould tooling and control of thermal parameters and motor rotation speeds. The integrally-heated tooling, as shown in Fig. 5, allows for tight control of processing parameters giving good dimensional accuracy of the component part and minimal energy consumption [36].

The purpose of this study is to investigate the control of void volume fractions through the manipulation of processing parameters such as temperature, hold times and cooling rates [37]. The sides of the box-shaped mould are segregated into different heating channels so that optimal control of temperatures throughout the mould can be achieved. Temperature distributions in rotational moulding of polymers are known to affect part thickness [13].

3.2. Hot Plate Apparatus

A second method of part production, consisting of a hot plate apparatus was also used. This method produces parts by supplying heat to the bottom of an aluminium plate causing the powder on the surface to melt and coalesce where it is in contact with the plate, Fig. 6. The hot-plate apparatus has been used previously for specimen preparation in void volume fraction studies to mimic rotationally moulded parts [38]. The hot plate simulates the external heating supplied to the powder and melts the polymer component in a method that is similar to that of rotomoulding processes as it also creates voids in the part cross section. Artificial cooling operations were provided by a fan which was directed at the bottom of the plate. This also imitates the effect of cooling provided by the continual rotation of the mould after all heating operations have ceased. Temperature readings were taken from the plate surface beside the sample with a thermocouple covered with high temperature sealant tape to better analyse the temperature where the powder was in contact with the plate wall.

The void volume fraction is undoubtedly affected also by heating rate. In order to preclude the effect of heating rate from the present study, the heating rate has been kept approximately constant in the hot-plate and rotomoulding tests carried out here, as tabulated in Table 2. A comparison of hot plate test data to rotomoulded sample data is presented below.

3.3. Specimen Characterisation

A void content analysis was undertaken to examine the effects of heating parameters on void formation and to determine the size of void radii for mass diffusion modelling. An OLYMPUS BX51M table-top microscope in conjunction with OLYMPUS Stream image analysis software was used to characterise samples through the use of binary imaging techniques. Samples were cut from the original material where the mould surface side was imaged for void volume fraction and void radius measurements. Voids were clearly visible and so no extensive preparation methods were needed. The image analysis software differentiates pixel colours within the microscopy image and allows the user to set two colour bands into which the different pixel colours will fall. The void volume fraction can be obtained by calculating the relative area in each of the two colour bands set in the image. The average radius of voids contained within the image can also be obtained, with the software identifying pixels in the same band which are connected together. The maximum straight line length between two such connected pixels can then be obtained with an output of

average void radii being achieved. The correlated data is then available for analysis giving important information such as void volume fraction and the radius of each individual void present.

3.4. Test Conditions

A programme of tests for void volume fraction and average void size was undertaken for hot plate moulded and rotomoulded samples. Three different moulding temperatures (150 ^{o}C, 170 ^{o}C, 190 ^{o}C) were used to produce three samples on the hot plate for each temperature. These samples were analysed for void volume fraction and average void radius. All samples had a nominal thickness of 3.0 mm. Subsequently, three box components were rotomoulded at three similar temperatures (160 ^{o}C, 170 ^{o}C, 180 ^{o}C), again with nominal thicknesses of 4.0 mm. These samples were analysed for void volume fraction and average void size, with a comparison drawn with earlier hot plate moulded samples. Two additional boxes of increased thickness were rotomoulded at the higher temperature of 180 ^{o}C to determine the effect of nominal thickness. This was achieved by using larger powder masses for each case.

4. EXPERIMENTAL RESULTS

Four images from each of three different samples for one moulding temperature were taken and analysed for void volume fraction measurements in the hot plate moulded parts (Fig. 7). Fig. 8 shows the measured relationship between average void fraction and corresponding moulding temperature. A linear trend is observed, with increased temperatures leading to a decrease of void volume fraction. Fig. 9 shows the relationship between mean void radii and void volume fraction. A relatively high volume fraction of relatively smaller voids was formed at the lower moulding temperatures and a lower volume fraction of the relatively larger voids were formed at higher temperatures.

A thermal imaging camera was used to measure the temperature distribution in the rotational mould tool, Fig. 10. Eight images of polymer samples, Fig. 11, taken from each side of the box component (Fig. 12) were taken and measurements for void volume fraction and void size were compiled. Fig. 13 shows a similar trend to hot plate moulded samples with a decrease in void volume fraction observed for parts moulded at higher moulding temperatures. Fig. 14 shows that the average void radius was also found to increase (somewhat) with increased moulding temperature and reduced void volume fraction in a broadly similar trend to that of the hot plate moulded samples.

The final analysis undertaken for the rotomoulded parts was to analyse the void volume fraction trends in rotomoulded parts as a result of changes in the thickness of the wall cross

section, using the two boxes rotomoulded at 180 ^{o}C, with resulting average wall thicknesses of 5.5 mm and 6.0 mm. In a comparison to the earlier rotomoulded sample at 180 ^{o}C, the thicker boxes exhibited a further reduction in void volume fraction, as shown in Fig. 15. This is attributed here primarily to the increased diffusion of voids at higher temperatures and is further accentuated by the longer time period required to reach the higher moulding temperature for higher powder masses. The average void size was found to be negligibly affected by wall thickness.

5. FINITE ELEMENT ANALYSIS RESULTS

Fig. 16 shows the FE models developed using mean void radii of between 100 µm and 200 µm. A range of void volume fractions were used to study the effect of void morphology on permeability. In the FE results of Fig. 17, the lighter regions indicate significantly higher mass flow rates and darker regions indicate regions of reduced mass flow rate. It can be seen that the diffusion path tends to follow the void pattern, as this results in the path of least resistance for the mass flow, as discussed earlier. The lower diffusion coefficient of the air voids contained within the liner increases the mass flow, which will increase fuel leakage and will be detrimental in cryogenic fuel storage applications. It is clear that the voids significantly affect the mass flow pattern, leading to a concentration of the flow through the void and allowing for an easier path for mass flow to occur.

The predicted permeability results for the random void distribution models are shown in Fig. 18. An increase in void volume fraction is predicted to significantly increase permeability, with multiple data points (corresponding to different random distributions of voids) from the FE model displaying this trend. The smaller (100 μm) voids are predicted to have a higher permeability then the larger (200 μm) voids for similar volume fractions. The smaller voids can distribute more uniformly throughout the model, thus creating a more continuous path which increases permeability. These FE results are compared to the heterogeneous diffusion models described in Section 2.2. The FE model trend follows that of the predictive equations. The latter only give one data point for each volume fraction and this lies within the FE predicted range, due to the random distributions analysed. The FE trend agrees more closely with the Maxwell and Lewis-Nielsen models than the Bruggeman model. The FE model accounts for void morphology statistics and this provides a statistical range for permeability.

From Fig. 18, the FE predicted permeabilities for the higher moulding temperature void volume fraction of 1.5 % with 200 μm voids and the lower moulding temperature void volume fraction of 5.5 % with a void size of 100 μm are 2.55×10^{-7} mol/m^2.s and 2.9×10^{-7} mol/m^2.s respectively. This indicates that higher moulding temperature is beneficial for reduced predicted permeability.

Another factor which can significantly affect permeability is part thickness (or powder mass). In order for designers to be able to assess the implications of increased part size and weight vis-à-vis reduced permeability, it is important to understand the effect of thickness on permeability for realistic void morphologies. In Fig. 19 a study of voids in rotomoulded samples of varying thickness has been conducted for polyethylene components formed at 180 ^{o}C by using different total powder weights. The V_f = 0% trend line is effectively a Fick's Law prediction of thickness effects. The 5% and 10% V_f trend lines, which show multiple data points, correspond to different random distributions of voids for each thickness value, showing that:

1. Even with realistic void morphologies a Fick's law trend is predicted to persist for each V_f shown.
2. The effect of random void distributions is relatively small for a given V_f and thickness.

Fig. 19 also shows that for the zero void volume fraction, the permeability is less than the quoted target value of 2.23 x 10^{-7} mol/m^{2}s (mentioned earlier for COPV applications) for thicknesses greater than 3.5 mm. Also shown in Fig. 19 are separate predictions for the R3, R4 and R5 cases from Table 2. These specific predictions use the measured values of V_f for their corresponding thickness. In all three cases the predicted permeability is seen to be

below the target maximum permissible permeability. This shows how a combination of increased moulding temperatures (above 180 ^{o}C) and increased wall thickness (powder mass) can be used to control permeability.

6. PERMEABILITY PREDICTION METHODOLOGY

As has been shown by the previous hot plate and rotomoulding results, good correlation has been found between void volume fractions and void sizes in both manufacturing methods. This suggests that hot plate results can be used to estimate void volume fraction parameters for rotomoulded polyethylene components. The relationship between moulding temperature and void volume fraction follows a linear trend for the hot plate samples, where the void volume fractions, V_f, can be related to hold temperature, T, as follows:

$$V_f = aT + b \tag{6}$$

where a and b are constants with values of -0.000825 and 0.17358, respectively. The measured relationship between void volume fraction, V_f, and average void radius, R_v, for a range of moulding temperatures can also be interpreted for the hot plate samples. It is clear that increased processing temperatures lead to an increase in average void size and a decrease in average void volume fraction, as one would expect [37]. The reduced void volume fraction at increased temperatures can be attributed to the diffusion of voids due to

thermal diffusion effects [39]. The relationship between average void radius, R_v, and void volume fraction, V_f, can be represented by the following equation:

$$R_v = \alpha(\ln(V_f) + \beta) \quad (7)$$

where α and β are constants with values of -66.225 and 1.33, respectively, for the polymer and processing conditions investigated here. This suggests the possibility of predicting void volume fraction and size in rotomoulded parts based on the measured (hot-plate) relationships between moulding temperature, void volume fraction and average void size.

These predictive equations are applied here to the rotational moulding process presented above, as follows (see Fig. 20):

1. A part (Fig. 12) is rotationally moulded and material samples are extracted from selected locations for void analysis. The void analyses are conducted to characterise the void sizes and volume fractions for the selected locations.

2. The temperature of the mould is measured, using the full-field thermal imaging technique described. The maximum temperatures during the moulding cycles for the locations corresponding to those at which void analyses were conducted in step 1 are identified.

3. Eq. 6 is applied to predict the void volume fraction, based on this temperature.

4. Eq. 7 is applied to predict the mean void radius, based on the void volume fraction from Step 3.

5. Mass diffusion models are created for the defined parameters and, using Eq. 1, the rotomoulded liner's permeability is predicted.

This methodology is applied here to rotomoulded samples formed at three different temperatures. Table 4 shows the comparison of predicted (from hot plate data) and measured (rotationally moulded) values for the three temperatures. This predictive approach shows particularly good accuracy at the higher moulding temperatures. The derived predictive equations have slightly under- and over-predicted the value of V_f at 170 ^{o}C and 180 ^{o}C respectively but are still accurate to within 10%. The predictive equations have also under-predicted the value of V_f for the 160 ^{o}C samples but are accurate to within approximately 15%. R_v predictions are slightly over-predicted at 160 ^{o}C and 180 ^{o}C but are within 5% of measured values. The predicted R_v value for the 170 ^{o}C samples was also under-predicted by roughly 8%.

The specific forms of Eq. 6 and 7, although giving a reasonably good fit over the full temperature range, do not necessarily capture the detailed variations of R_v and V_f with temperature. In particular the predicted equations over-predict the change in R_v between

170 ^{o}C and 180 ^{o}C and, vis-à-vis the measured change, significantly under-predict the change in R_v between 160 ^{o}C and 170 ^{o}C relative to the measured increase.

However, in the present work, the effect of temperature is first captured via the effect on V_f which is linked to R_v through Eq. 7. The latter over- and under-predictions in R_v with respect to temperature changes can be traced back to imperfections in the linear fit of V_f to temperature in Eq. 6.

Hence a more complex equation (e.g. non-linear) between V_f and temperature would help to achieve an even better accuracy of predictions for V_f and R_v with respect to changes in temperature. Nonetheless, the errors of the predictions are less than 8% for average void radius and less than 15% for void volume fraction predictions. This methodology will facilitate identification of optimum processing temperatures for the production of polymer liners with acceptable void morphologies for predicted permeability.

7. CONCLUSIONS

Moulding temperature for rotomoulded components has been shown to have a significant effect on void volume fraction, with higher temperatures giving lower void volume fractions and hence lower predicted permeabilities. Nominal wall thickness (powder mass) has also been shown to have a significant effect on void volume fraction for rotomoulded components, with larger thicknesses giving a lower predicted permeability.

A simplified predictive methodology, based on hot plate measurements, for void volume fraction and void radius depending on temperature, has been shown to give reasonably good correlation with rotomoulded components.

FE mass diffusion models predict permeability results which are consistent with theoretical models. The FE method presented is superior in providing a statistical range for permeability based on measured void morphology statistics.

The present work represents an important step towards a combined experimental and modelling methodology for development of inexpensive, low permeability polymer liners. Current ongoing work is focused on permeability testing of prospective materials for candidate selection for COPV liners.

8. ACKNOWLEDGEMENTS

The authors would like to thank the Irish Research Council (IRC) and the European Space Agency (ESA) for joint funding of this research under the Network Partnering Initiative (NPI), and would like to acknowledge the help and technical support provided by ÉireComposites Teo., specifically that of P.J. Feerick, and the technical staff at NUI Galway.

9. REFERENCES

1. Grimes-Ledesma LR. et al. A Comparison of Various Stress Rupture Life Modules for Orbiter Composite Pressure Vessels and Confidence Intervals, *9th Joint FAA/DoD/NASA Aging Aircraft Conference,* Atlanta, USA, 2006.
2. Tam W. et al. Hybrid Propellant Tanks for Spacecraft and Launch Vehicles, *39th AIAA Propulsion Conference*, Alabama, USA, 2003. AIAA2003-4607.
3. Kawahara G. et al. Titanium Lined, Carbon Composite Overwrapped Pressure Vessel, *Proc. 32nd AIAA Conference,* Florida, USA, 1996.
4. Thesken JC. et al. Composite Overwrap Pressure Vessels: Mechanics and Stress Rupture Lifing Philosophy, *NASA/TM—2009-215683,* Ohio Aerospace Institute, Brook Park, Ohio, USA, 2009.
5. Tam W. et al. Review and History of ATK Space Systems Commerce – The Past 15 Years. *ATK Space Systems Commerce Division*, 2008.
6. McLaughlan PB. et al. Composite Overwrapped Pressure Vessels, A Primer - *NASA/SP–2011–573*, Johnson Space Center, Houston, Texas, USA, 2011.
7. Claudel S. et al. Advanced and Affordable Thermoplastic Based Composite Tank for Cryogenic Fluid Storage. *SAMPE Conference*, Washington State Convention Center, Seattle, USA, 2010.
8. Benedic F. et al. Helium High Pressure Tanks at EADS Space Transportation New Technology with Thermoplastic Liner. Report, *EADS ST,* France, 2005.

9. Mataloni A. et al. Technology Research Program; Elastomeric Liner for Cryogenic Tank Application. Report, *AVIO – Comprensorio BPD, NTEESA10007 Iss.:2,* Italy, 2005.
10. McEvoy JP. et al. Simulation of the Stretch Blow Molding Process of PET Bottles, *Adv Polym Tech* 1998; 17: 4: 339-352.
11. Awaja F. et al. Injection stretch blow moulding process of reactive extruded recycled PET and virgin PET blends, *Eur Polym J* 2005; 41: 2614–2634.
12. Grogan DM. et al. An XFEM-based methodology for fatigue delamination and permeability of composites, *Compos Struct* 2014; 107: 205-218.
13. Crawford RJ. et al. *Practical Guide to Rotational Moulding,* Rapra Technology Limited, Queen's University, Belfast, 2003.
14. Crank J. *The Mathematics of Diffusion,* 2nd Edition, Brunel University, Clarendon Press, Oxford, England, 1975.
15. Fick AE. Ueber Diffusion, *Ann Phys* 1855; 170: 1: 59–86.
16. Flaconnéche B. et al. Permeability, Diffusion and Solubility of Gases in Polyethylene, Polyamide 11 and Poly(vinylidene fluoride), *Oil Gas Sci Technol* 2001; 56: 3: 261-278.
17. Cengel YA. *Heat and Mass Transfer A Practical Approach*, 3rd Edition, McGraw-Hill, University of Nevada, Reno, USA, 2006.
18. Klopffer MH. et al. Transport Properties of Gases in Polymers: Bibliographic Review, *Oil Gas Sci Technol* 2001; 56: 3: 223-244.

19. Comyn J. *Polymer Permeability,* 1st Edition, Chapman & Hall, London, UK, 1985.
20. Maxwell C. Treatise on Electricity and Magnetism, Vol. 1. Oxford University Press, London, 1873.
21. Gonzo EE. et al. Estimating models for predicting effective permeability of mixed matrix membranes, *J Membrane Sci* 2006; 277: 46–54.
22. Bruggeman DAG. Calculation of various physical constants of heterogeneous substances. I. dielectric constant and conductivity of the mixed body of isotropic substances. *Ann Phys* 1935; 416: 7: 636 – 664.
23. Lewis TB. et al. Dynamic mechanical properties of particulate-filled composites. *J Appl Polym Sci* 1970; 14: 6: 1449 – 1471.
24. Nielsen L. Thermal conductivity of particulate-filled composites. *J Appl Polym Sci* 1973; 17: 3819 – 3820.
25. Bouma RH. et al. Permeation through a heterogeneous membrane: the effect of the dispersed phase. *J Membrane Sci* 1997; 128: 141-149.
26. Pal R. Permeation models for mixed matrix membranes. *J Colloid Interf Sci* 2008; 317: 191-198.
27. Hashemifard SA. et al. Prediction of gas permeability in mixed matrix membranes using theoretical models. *J Membrane Sci* 2010; 347: 53-61.

28. Hashemifard SA. et al. A new theoretical gas permeability model using resistance modeling for mixed matrix membrane systems. *J Membrane Sci* 2010; 350: 259-268.
29. Dassault Systèmes Simulia Corp. ABAQUS Analysis User's Manual 6.10. Providence, RI, USA, 2010.
30. ASTM D1434-82:2009. Standard Test Method for Determining Gas Permeability Characteristics of Plastic Film and Sheeting.
31. Nettles AT. Permeability Testing of Composite Material and Adhesive Bonds for the DC-XA Composite Feedline Program, *Marshall Space Flight Center*, Alabama, USA, 1995.
32. Oyama ST. et al. Theory of hydrogen permeability in nonporous silica membranes, *J Membrane Sci* 2004; 244: 45–53.
33. Choi S. Micromechanics, Fracture Mechanics and Gas Permeability of Composite Laminates for Cryogenic Storage Systems. PhD Thesis, University of Florida, USA, 2005.
34. Olson LG. et al. Rotational Moulding of Plastics: Comparison of simulation and Experimental Results for an Axisymmetric Mold, *Polym Eng Sci* 2000; 40: 8: 1758-1764.

35. Kearns M. et al. Comparison of cycle times and heating efficiency for direct electrically heated and conventional gas fired rotomoulding machines, *Rotation Magazine* 2004; 13: 6: 18-25.
36. Ó Brádaigh CM. et al. Electrically-Heated Ceramic Composite Tooling for Out-of-Autoclave Manufacturing of Large Composite Structures, *SAMPE Journal* 2011; 47: 4: 6-14.
37. Crawford RJ. Recent Advances in the Manufacture of Plastic Products by Rotomoulding, *J Mater Process Tech* 1996; 56: 263-271.
38. Spence AG. et al. Removal of Pinholes and Bubbles from Rotationally Moulded Products, *Proc IMechE Part B: J Engineering Manufacture* 1996; 210: 521-533.
39. Crawford RJ. *Rotational Moulding of Plastics,* 2nd Edition, Research Studies Press Ltd., England, 1996.

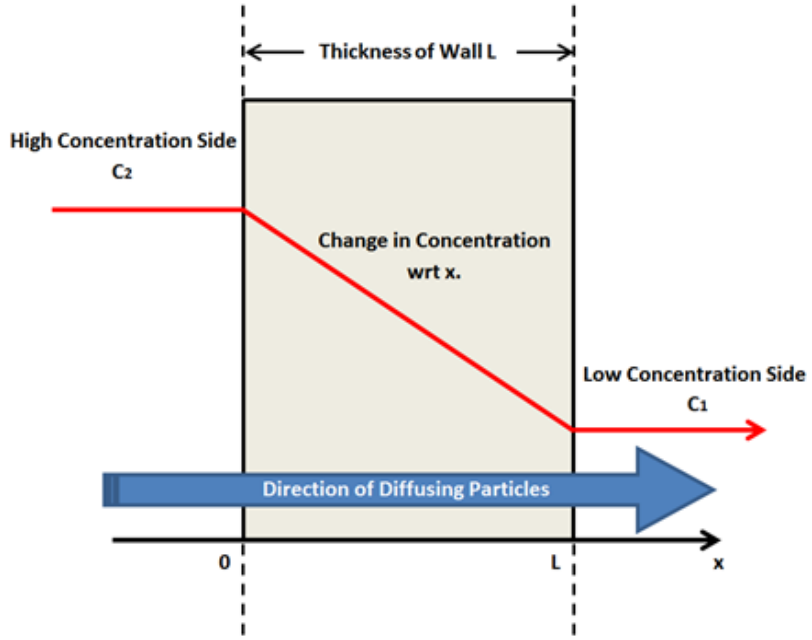

Figure 1. Visualisation of the parameters governing Fick's Law of diffusion.

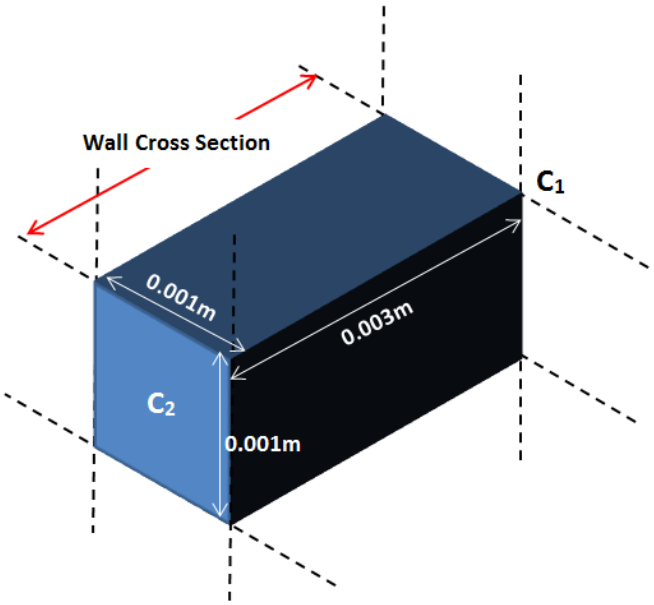

Figure 2. Schematic of the finite element model employed for the analysis of void contents in rotomoulded parts.

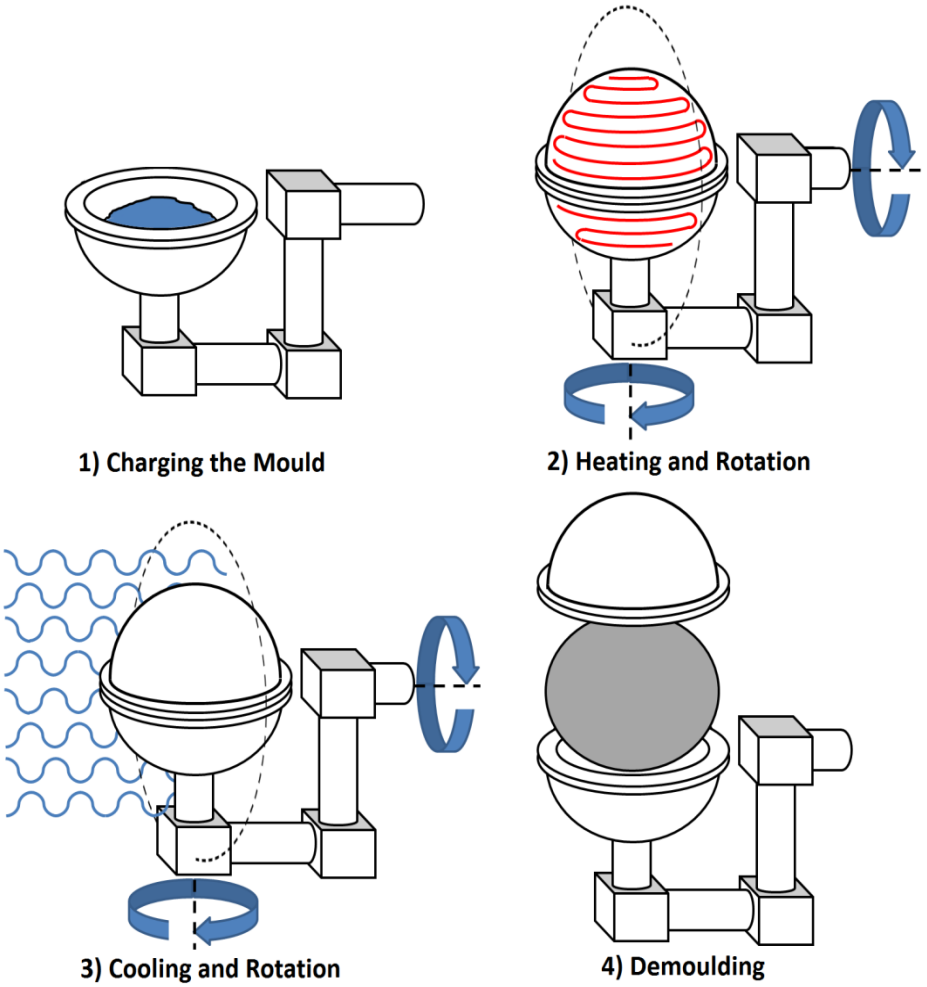

Figure 3. Main steps in rotational moulding.

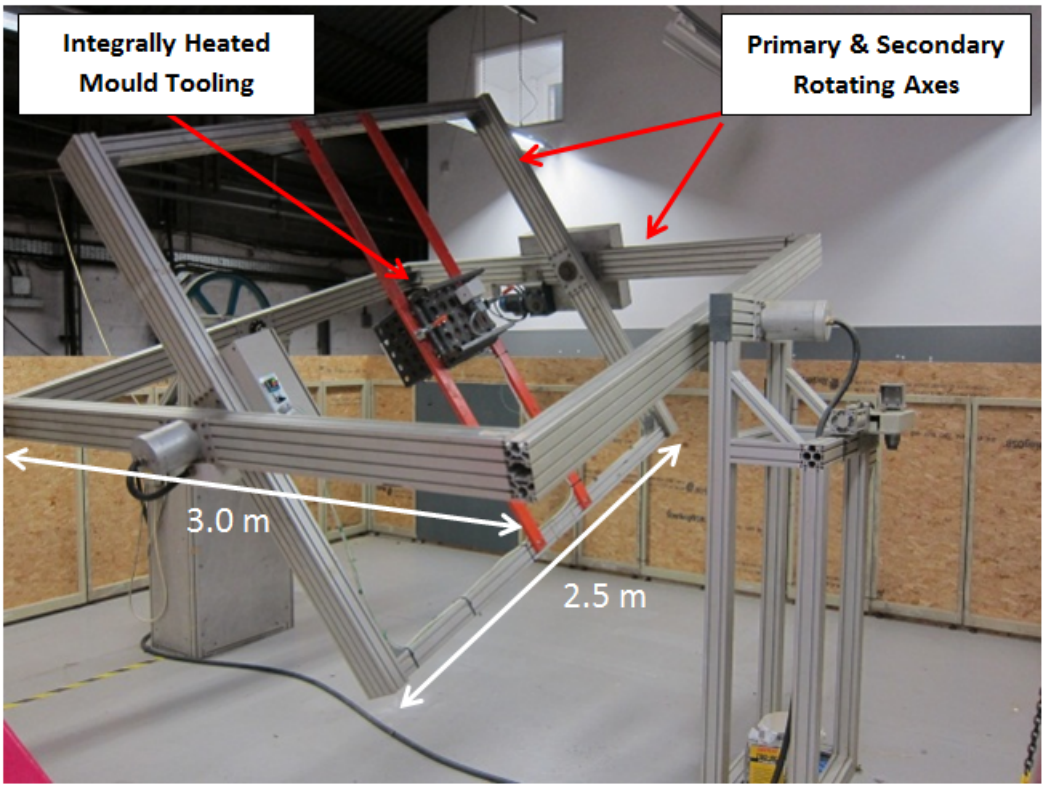

Figure 4. Photograph of the modified rotational moulding process developed for polymer liner production.

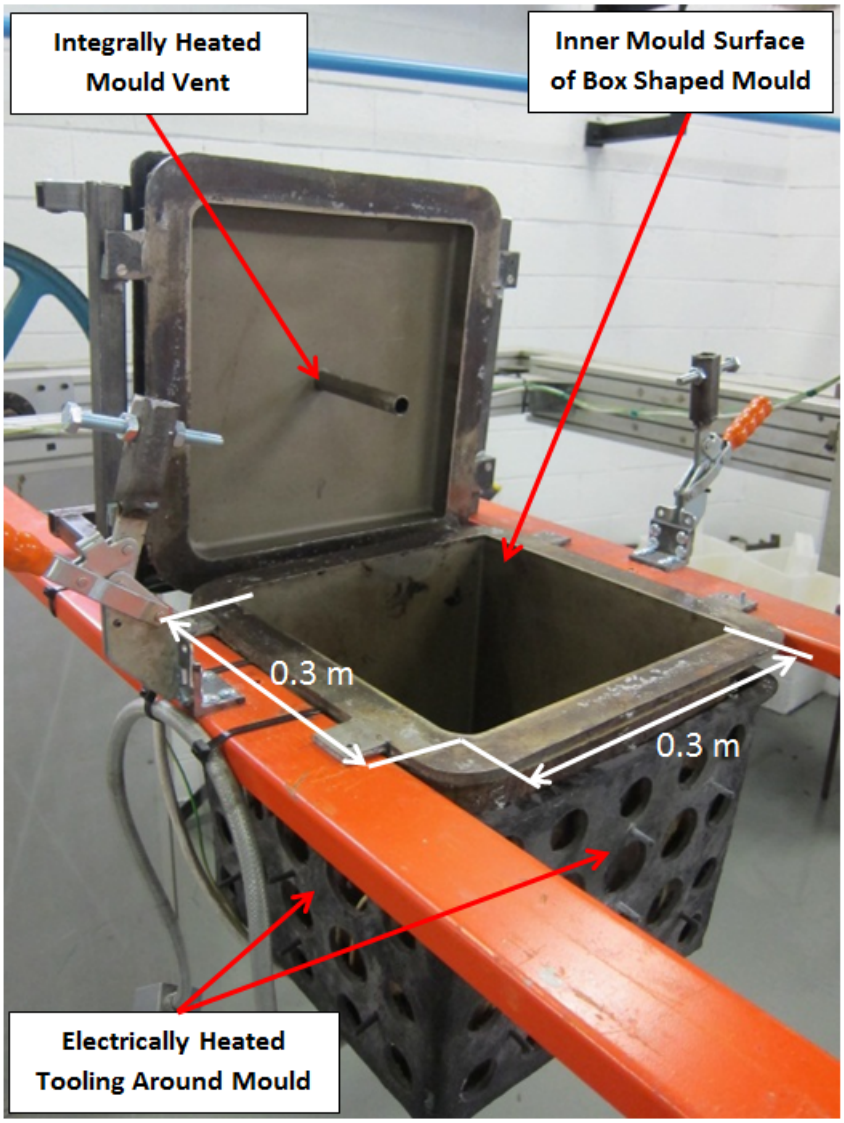

Figure 5. Photograph of the electrically heated mould tooling for the box-shaped mould.

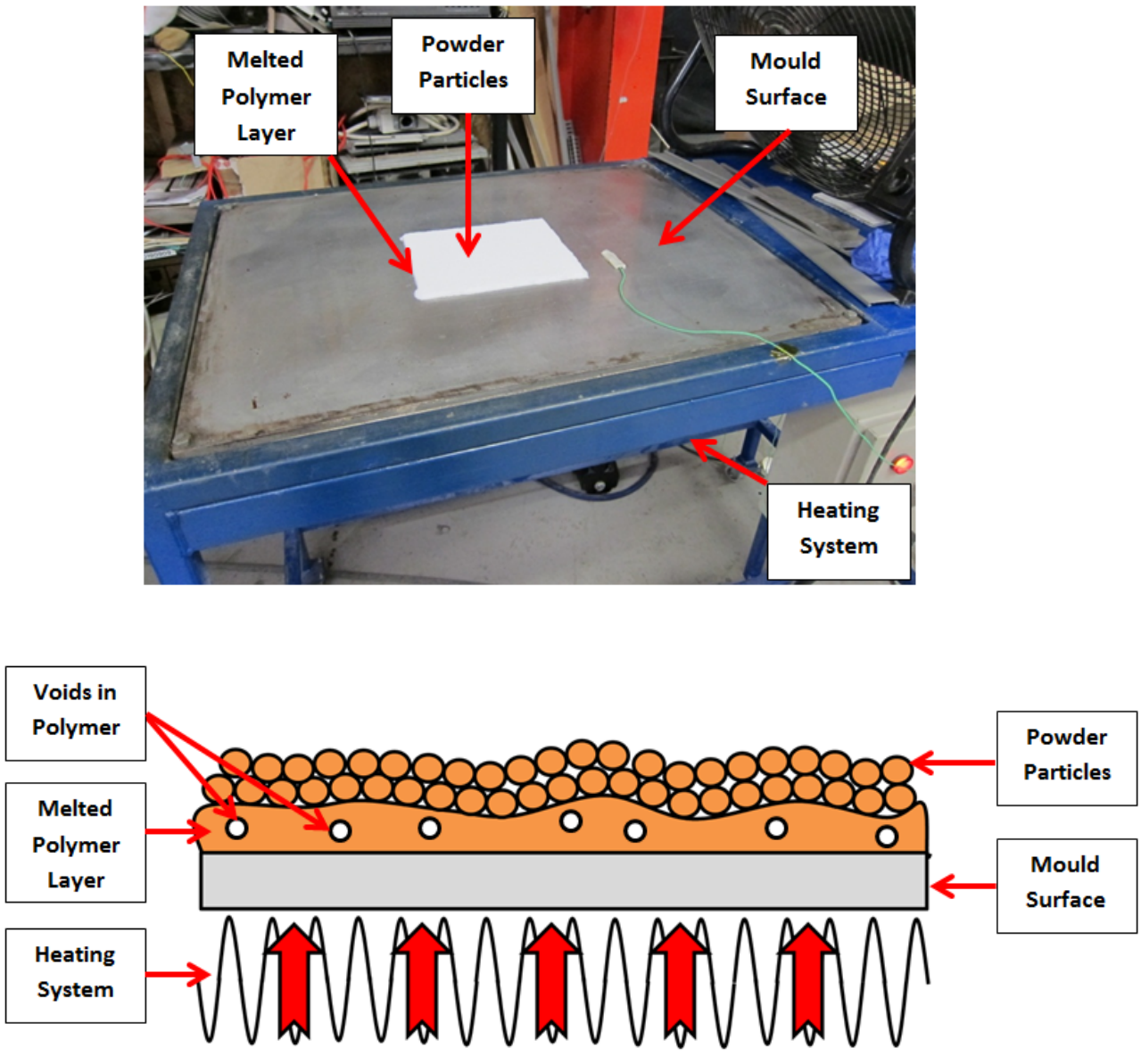

Figure 6. Dual image of the hot plate apparatus used for part formation accompanied by a schematic of the hot plate moulding process.

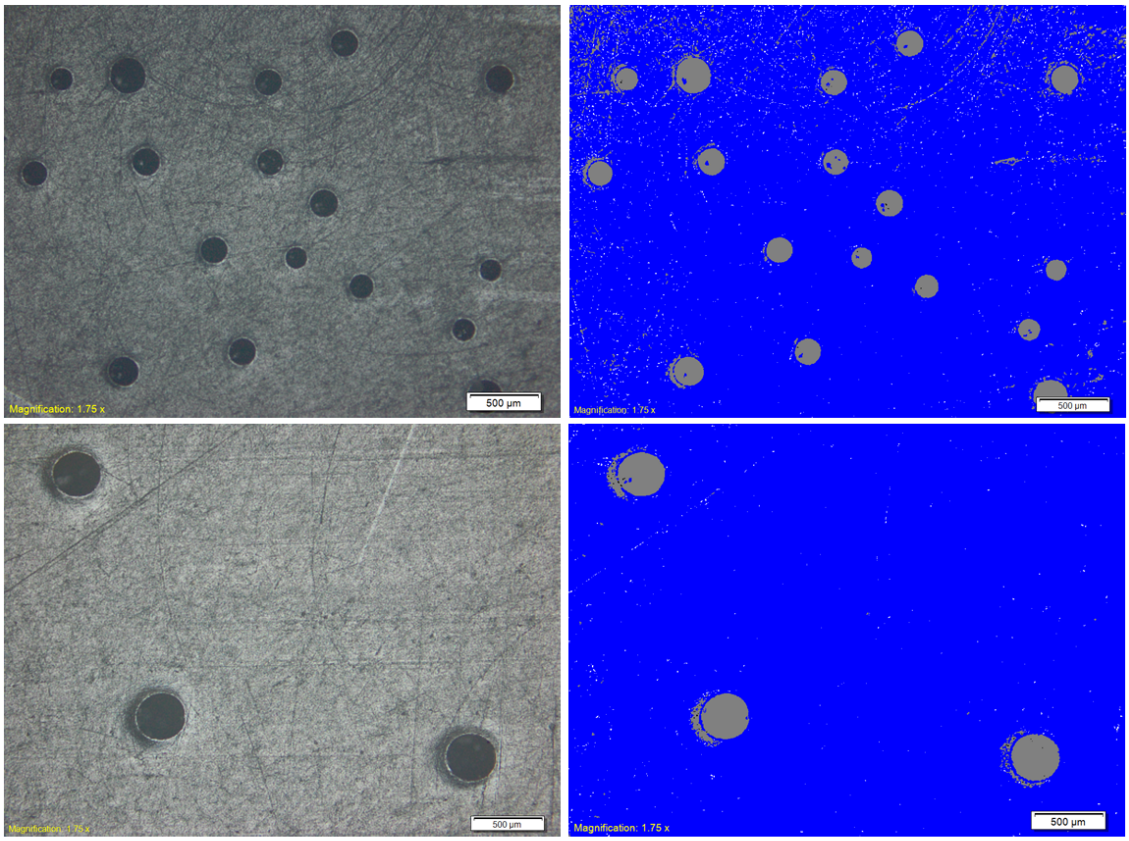

Figure 7. Collection of binary microscopy images for void volume fraction analysis in hot plate moulded parts.

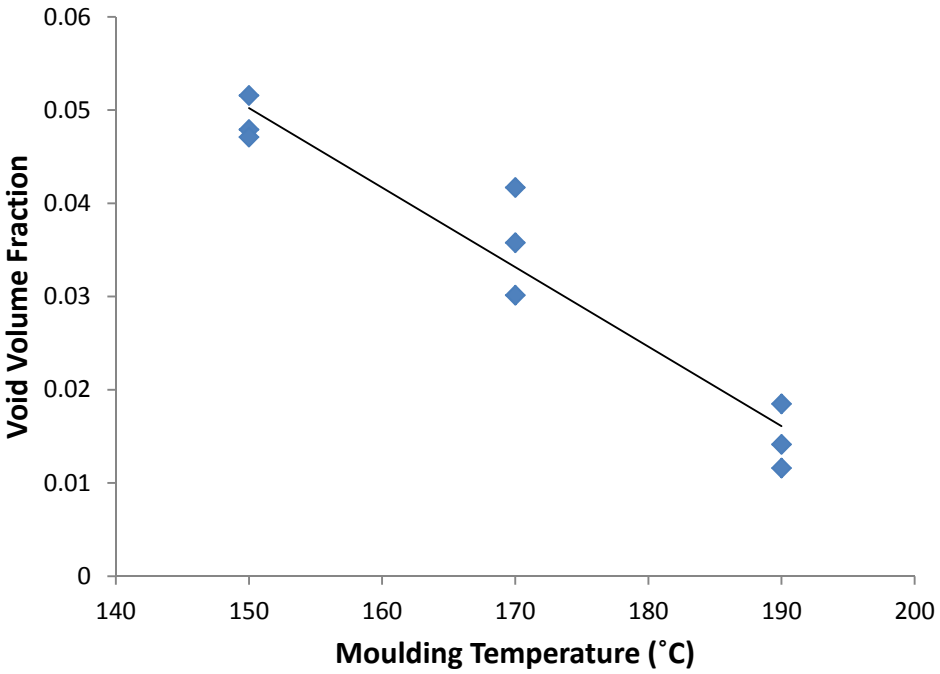

Figure 8. Measured effect of hot plate moulding temperature on void volume fraction in polyethylene samples.

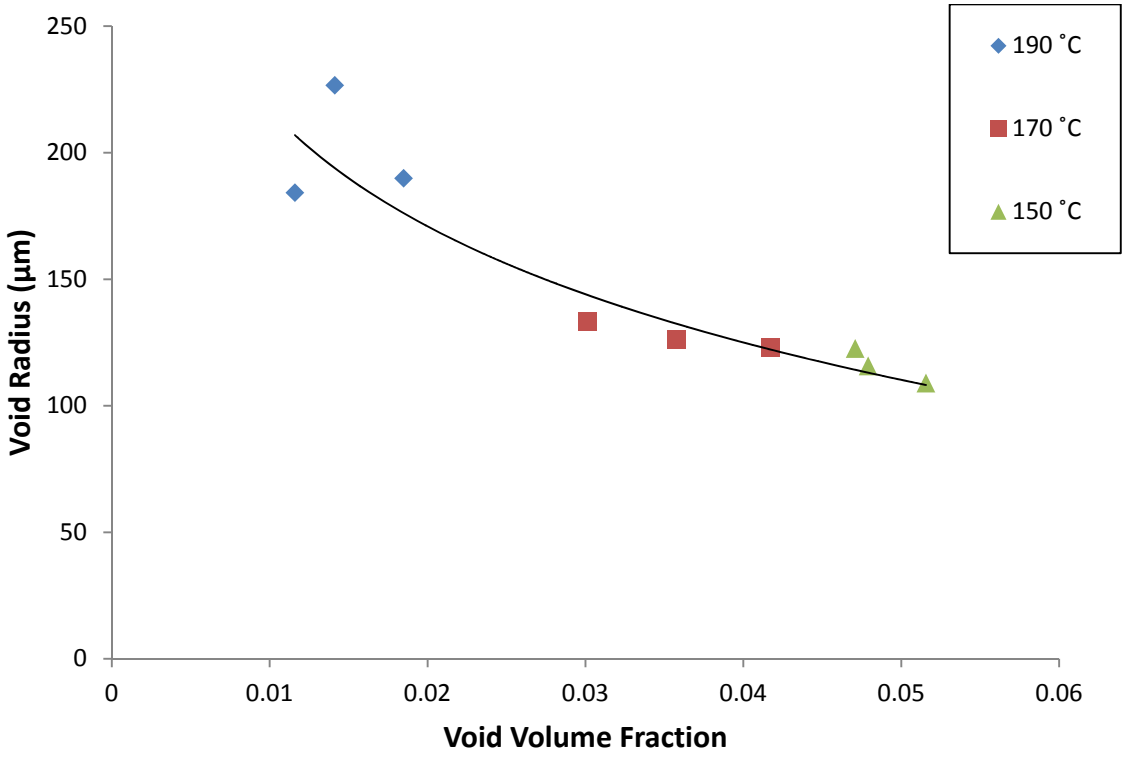

Figure 9. The effect of moulding temperature on void size and volume fraction for hot plate polyethylene samples.

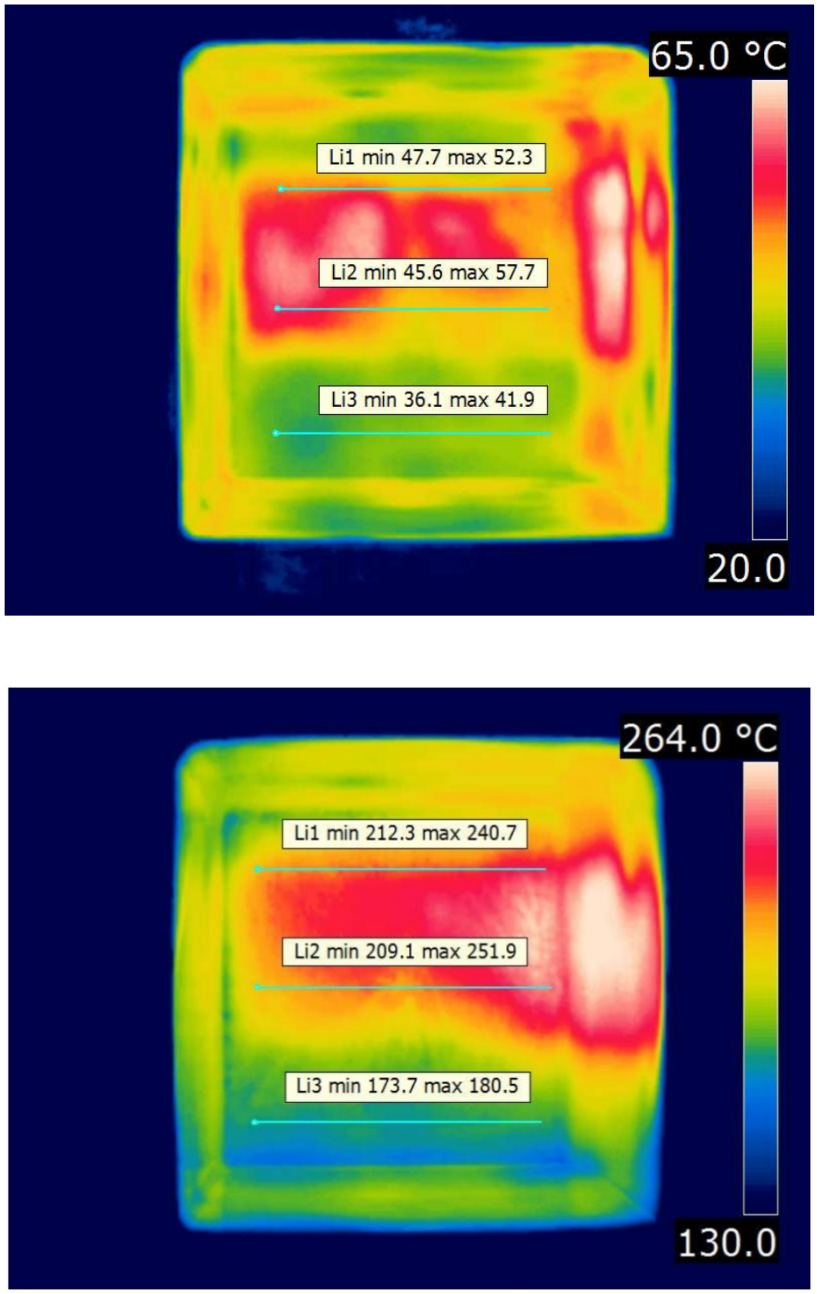

Figure 10. Thermal images of temperature distributions within the mould tooling during processing.

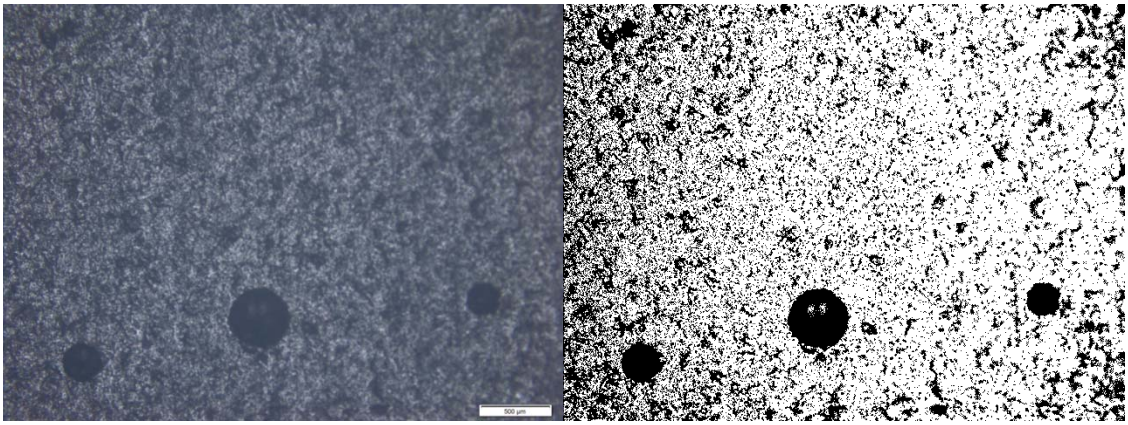

Figure 11. Microscopy image translated into a binary image for void volume fraction analysis of rotomoulded samples.

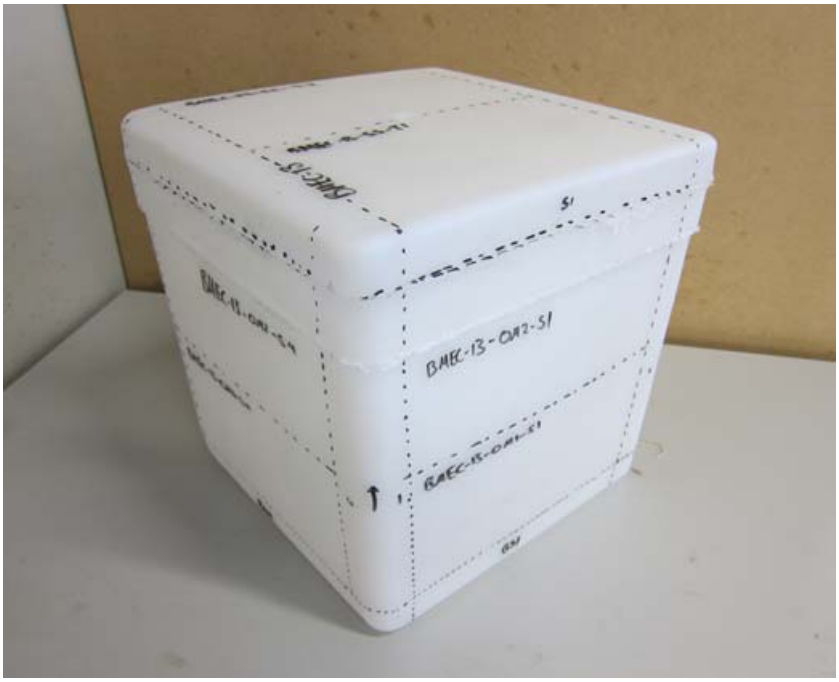

Figure 12. Photograph of sample rotomoulded parts.

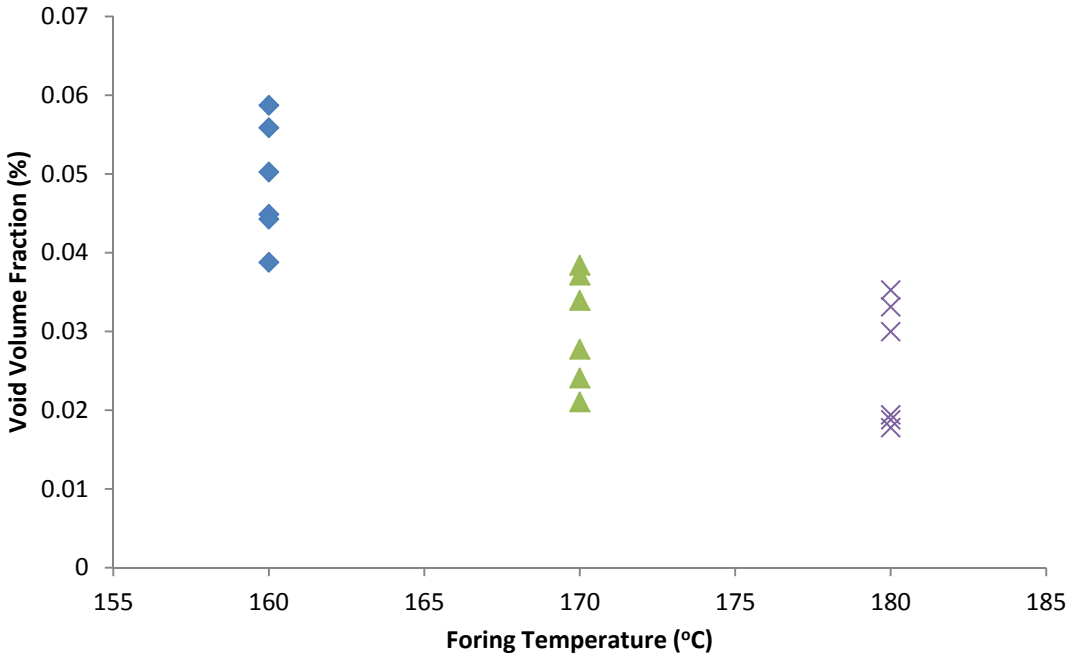

Figure 13. Measured effect of moulding temperatures on void volume fraction for rotomoulded samples.

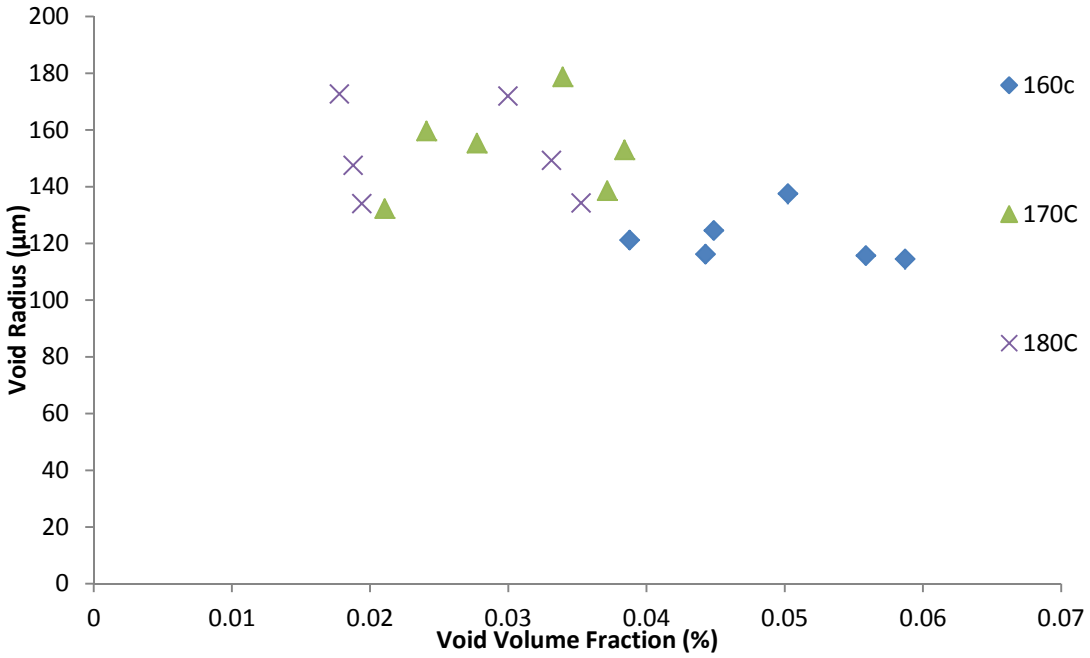

Figure 14. Measured relationship between void radius and void volume fraction for rotomoulded samples at different moulding temperatures.

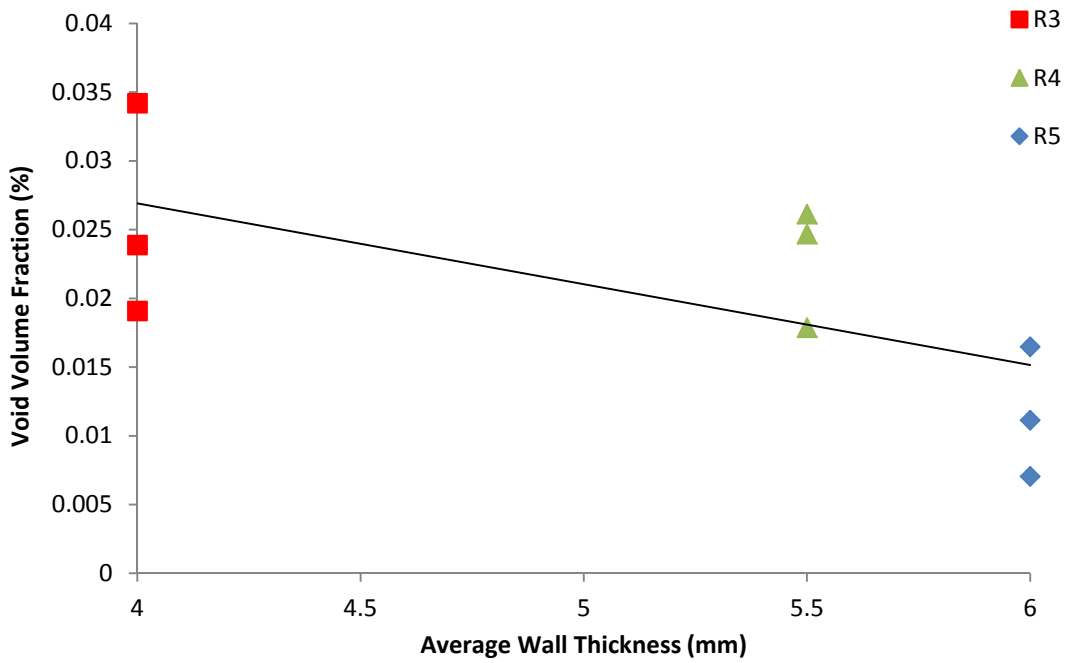

Figure 15. Changes in void volume fraction for rotomoulded component at 180^{o}C as a result of variations in nominal wall thickness.

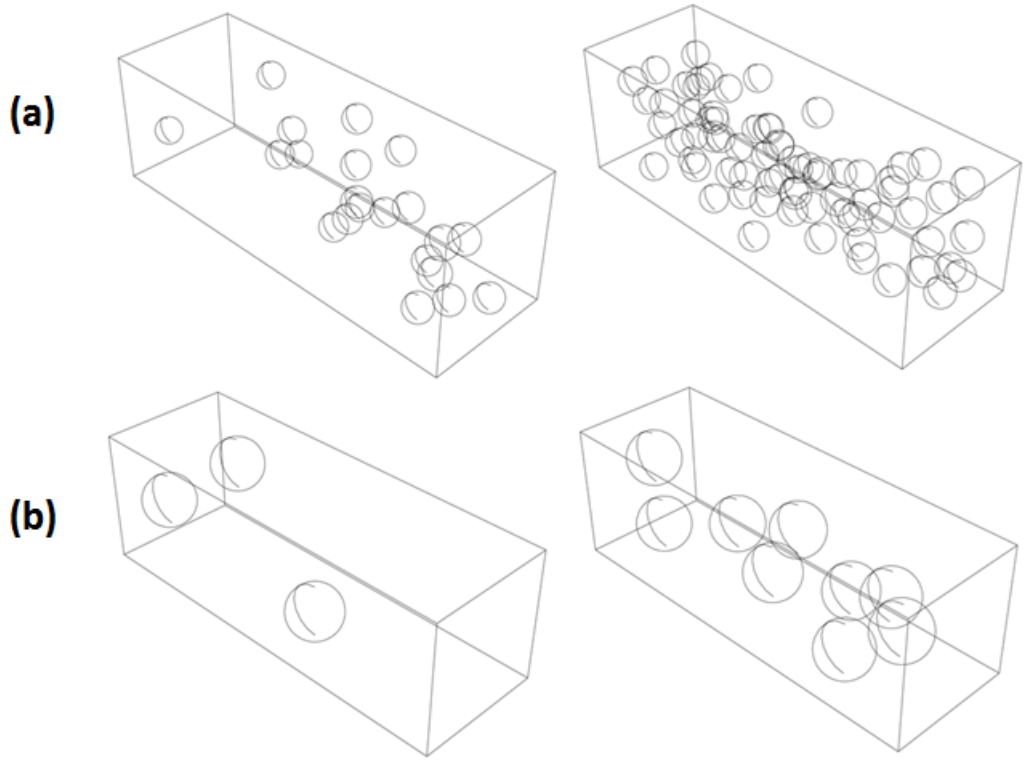

Figure 16. Random distributions of voids in the finite element model for (a) 100 µm voids and (b) 200 µm voids.

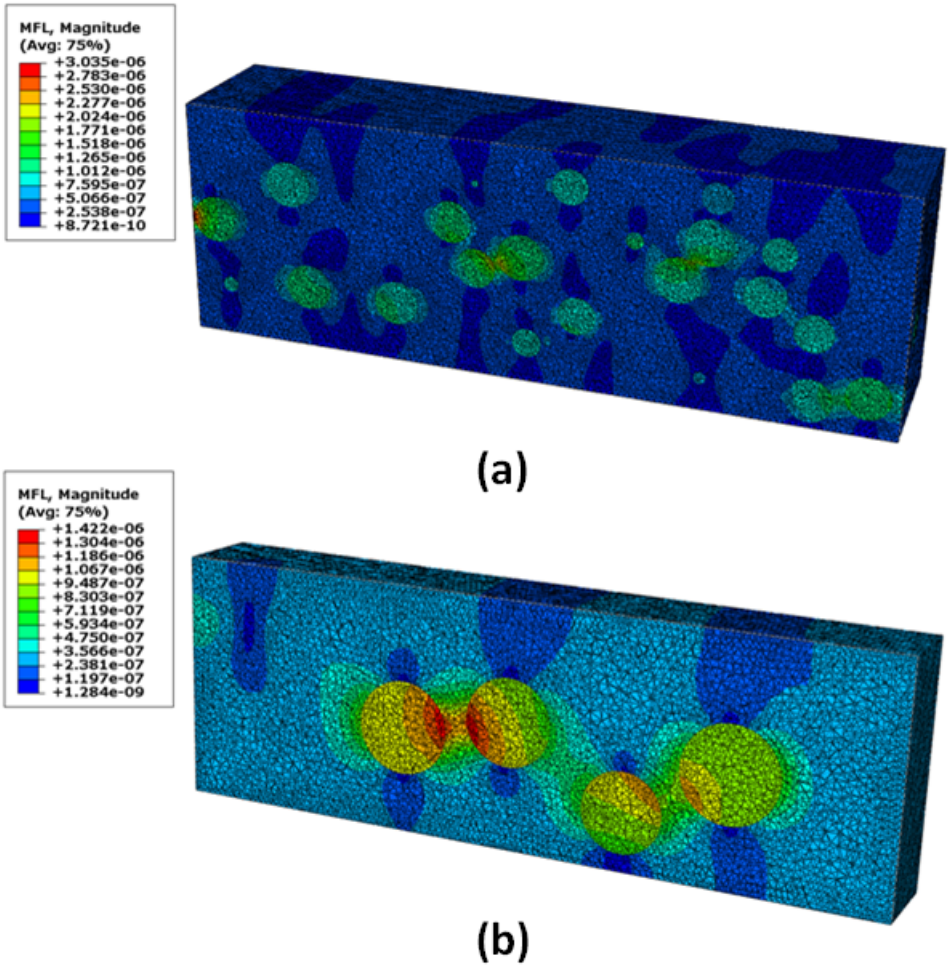

Figure 17. Finite element predictions of steady state helium mass flow with diffusion models of typical liner cross-sections. Random void distributions for (a) 100 µm void radii and (b) 200 µm void radii.

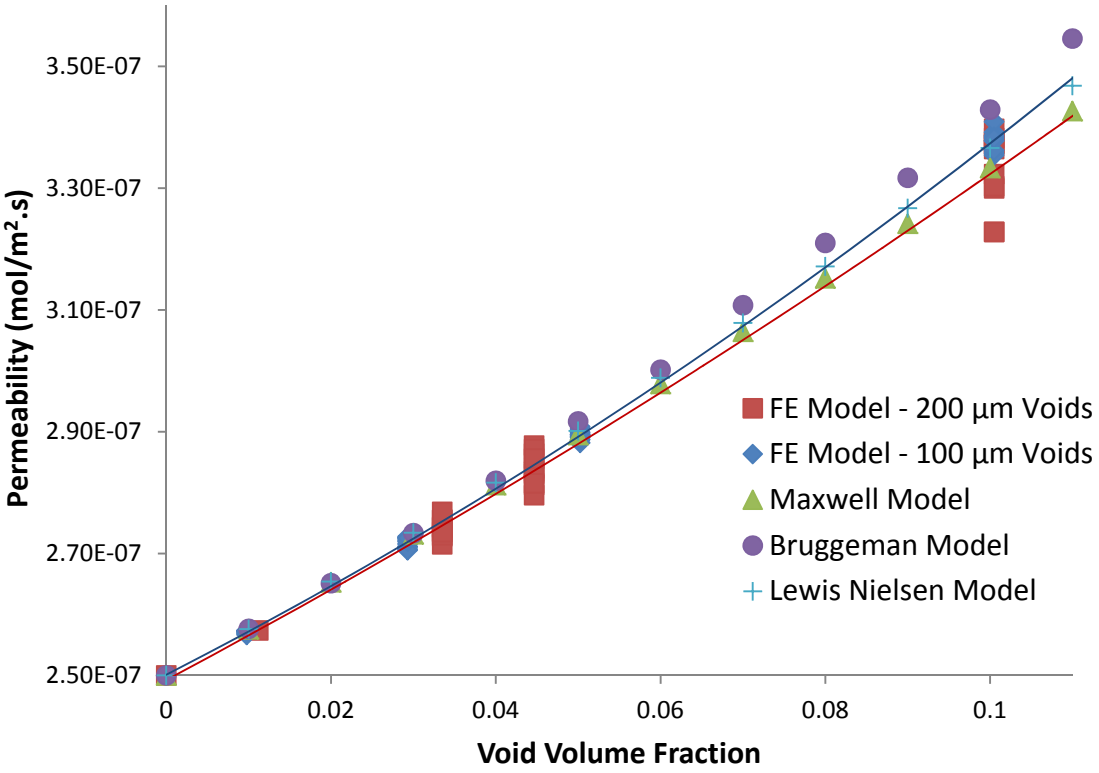

Figure 18. Comparison of finite element predicted and theoretically predicted mass flow rates for different void sizes as a function of the void volume fraction.

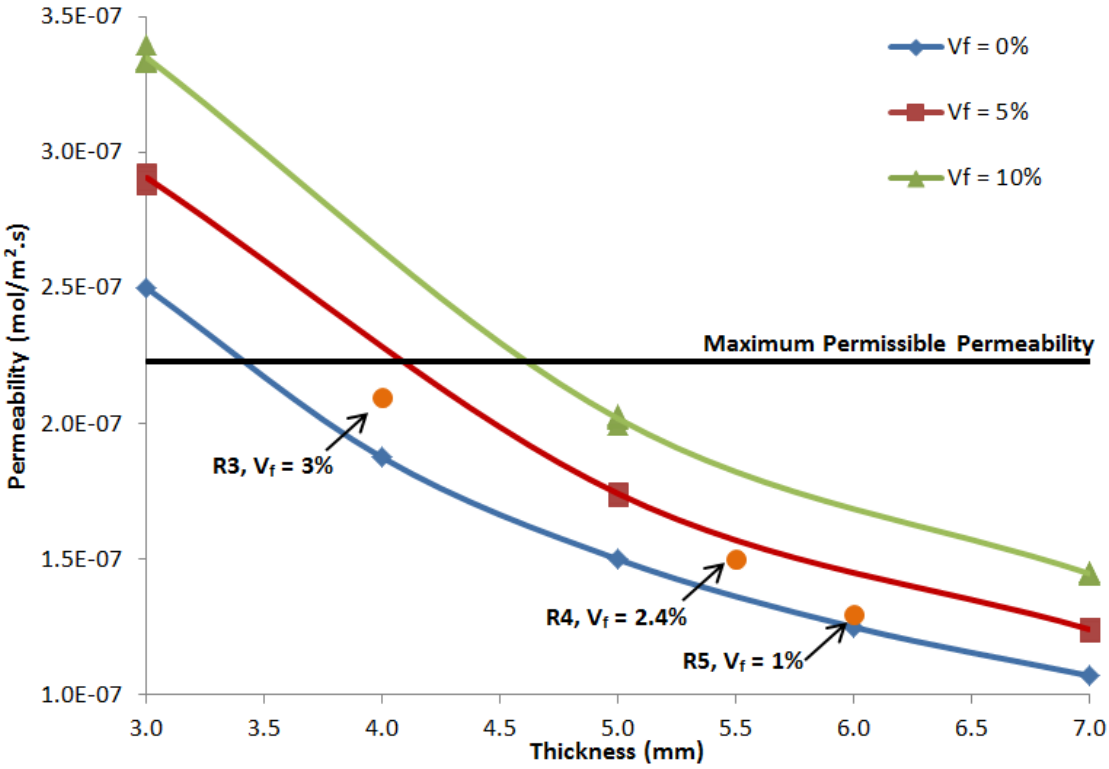

Figure 19. Finite element predicted effect of thickness on permeability for different void volume fractions.

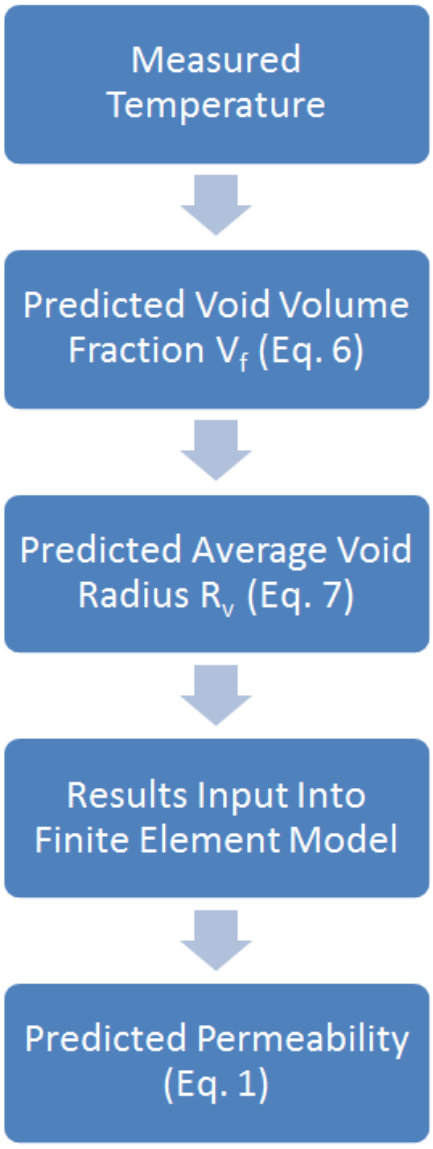

Figure 20. Flow chart for permeability prediction estimation method.

Table 1

Material Properties of Borealis Low Density Polyethylene Powder

Parameter	Borealis LDPE
Average Particle Size	300 - 400 µm
Melt Temperature	123 ^{o}C
Melt Flow Index	7.6 g/10min
Crystallinity	62%
Density (ρ)	0.94 g/cm^{3}

Table 2

Experimental data for the parts formed throughout this analysis.

Identifier	Hold Temperature (°C)	Manufacturing Method	Nominal Thickness (mm)	Heating Rate (°C/min)
H1	150	Hot Plate	3.0 - 4.0	10 - 15
H2	170	Hot Plate	3.0 - 4.0	10 - 15
H3	190	Hot Plate	3.0 - 4.0	10 - 15
R1	160	Rotomoulded	3.0 - 4.0	10 - 13
R2	170	Rotomoulded	3.0 - 4.0	10 - 13
R3	180	Rotomoulded	3.0 - 4.0	10 - 13
R4	180	Rotomoulded	5.0 - 5.5	10 - 13
R5	180	Rotomoulded	5.5 - 6.0	10 - 13

Table 3

Overview of values used for the finite element analysis [16 - 17].

Parameter	Finite Element Model
Model Dimensions	3 mm x 1 mm x 1 mm
Void Sizes (Radius)	100 – 200 µm
Diffusion Coefficient of Air	7.2×10^{-5} m^2/s
Diffusion Coefficient of PE (ρ=0.92 g/cm^{3})	1.4×10^{-9} m^2/s
Concentration Gradient	0.54 mol/m^{3}
Volume Fraction Analysed	0 - 10 %

Table 4

Comparison of measured and predicted mean of void distributions for rotomoulded samples at varying temperatures.

	Measured				Predicted		Error	Error
Temperature	Vf (%)	STDV (%)	Rv (µm)	STDV (µm)	Vf (%)	Rv (µm)	V_f (%)	R_v (%)
180°C	0.027	0.01	150	39.2	0.025	156	-7.1	+3.9
170°C	0.030	0.01	149	36.6	0.033	137	+9.8	-7.6
160°C	0.049	0.01	120	32.2	0.042	123	+14.8	+1.8

Note: the table above also shows the standard deviations (STDV) of the measured values.